Micro Structures in Thin Coating Layers: Micro Structure Evolution and Macroscopic Contact Angle

J. Dohmen[1], N. Grunewald[2], F. Otto[3], and M. Rumpf[4]

[1] Institut für Numerische Simulation, Universität Bonn, Nussallee 15, 53115 Bonn, `julia.dohmen@ins.uni-bonn.de`
[2] Institut für Angewandte Mathematik, Universität Bonn, Wegelerstr. 10, 53115 Bonn, `grunewald@iam.uni-bonn.de`
[3] Institut für Angewandte Mathematik, Universität Bonn, Wegelerstr. 10, 53115 Bonn, `otto@iam.uni-bonn.de`
[4] Institut für Numerische Simulation, Universität Bonn, Nussallee 15, 53115 Bonn, `martin.rumpf@ins.uni-bonn.de`

Summary. Micro structures of coating surfaces lead to new industrial applications. They allow to steer the wetting and dewetting behaviour of surfaces and in particular to enhance hydrophobicity. Here, we discuss the formation of micro structures in the drying process of a coating. Furthermore, for a given micro structured surface we show how to predict the effective contact angle of drops on the surface. At first, we derive a new approach for the simulation of micro structure evolution based on a gradient flow perspective for thin liquid films. This formulation includes a solvent dependent surface tension, viscosity and evaporation rate. In each time step of the resulting algorithm a semi implicit Rayleigh functional is minimized. The functional itself depends on the solution of a transport problem. We apply a finite difference discretization both for the functional and the transport process. As in PDE optimization a duality argument allows the efficient computation of descent directions. Next, given a certain micro structured coating we mathematically describe effective contact angles in different configurations and their impact on the macroscopic hydrophilic or hydrophobic surface properties. On periodic surfaces we aim at the computation of effective contact angles. This involves a geometric free boundary problem on the fundamental cell. Its solution describes vapor inclusions on the wetted surface. The free boundary problem is solved by a suitable composite finite element approach. Furthermore, we introduce a new model for the influence of micro structures on contact angle hysteresis. This model is adapted from elasto–plasticity and dry friction. It identifies stable contact angles not only as global or local energy minimizers but as configurations at which the energy landscape is not too steep.

Introduction

Micro structures in coatings are of great industrial relevance. They can be desirable and undesirable. On the one hand they might lead to rupture of a paint. On the other hand they can enhance hydrophobicity of the surface. Here we discuss two different aspects of these phenomena.

In Section 1 we consider a model for the formation of micro structures in a drying coating. These strucutures can for instance evolve from a non homogeneous solvent distribution in an originally flat coating. We model the coating by an adapted thin film model. It is based on a gradient flow model with solvent dependent viscosity, surface tension and evaporation rate, see section 1.1. This introduces Marangoni effects to the film which can lead to a structured film height but also counteract rupture. It also takes into account the solvent evaporation in a coating, which is fast at low film heights, due to a faster heating up. A third effect considered is the hardening, i.e. the temporal change of the viscosity of the coating. In Section 1.2 and 1.3 we introduce a numerical algorithm based on a semi implicit time discretization, which takes advantage of the gradient flow structure. In each time step a corresponding Rayleigh functional is minimized In Section 1.5 we show numerical results.

In the second part in Section 2 we discuss the implications of a structured surface to contact angles of macroscopic drops sitting on the surface. The micro structures highly influence the contact angle and thereby the sticking of the drop to the surface. One governing effect is the formation of vapor inclusions on the surface at a micro scale. This reduces the contact of the drop to the surface - hence, it rolls off easily. We introduce an algorithm in Section 2.1, which simulates the vapor inclusions in a periodic setup. The corresponding liquid vapor interface is a minimal surface with prescribed microscopic contact angle of the triple contact line. In the limit of small scale periodicity of the surface this enables the calculation of effective contact angles.

Finally, in Section 2.2 we consider the stability of drop configurations on the micro structured surface. A new model is introduced which determines the stability of effective contact angles. Their stability depends on the micro configuration of the drop, i.e. on the possible vapor inclusions. The model allows for intervals of stable contact angles (contact angle hysteresis). It is adapted from elasto–plasticity and dry friction, and assumes a configuration not only to be stable if it minimizes (locally) the relevant surface energy but also if the energy landscape at this configuration is not too steep. This leads to different hysteresis intervals for configurations with and without vapor inclusions. A change in the vapor configuration at the surface can explain the highly non monotone dependence of the hysteresis on the surface roughness, known since the sixties, [JD64], as well as more recent experiments.

1 Modeling and Simulation of the Micro Structure Formation in Thin Coatings

1.1 Modeling Thin Coatings as a Gradient Flow

We propose a simple model for coatings similar to the one considered in [HMO97], which in spite of its simplicity reproduces many of the interesting features known for a drying paint. We assume the paint to consist of two components, the non–volatile resin and the volatile solvent, whose concentration is given by s. Together they form a well–mixed fluid with height h. In the simulations we plot both the height (on the left) and the solvent concentration (on the right), see Figure 1. These are the two parameters describing the physical properties of the fluid:
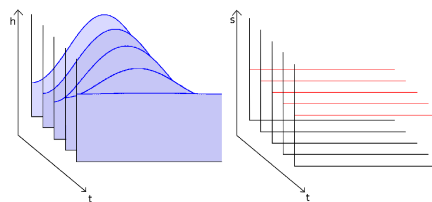

Fig. 1. A time evolution (back to front) of a coating is described by its height (on the left) and solvent concentration (on the right). Here the trivial case with constant Solvent Concentration is depicted.

The solvent concentration influences the viscosity μ (the drying coating becomes harder with descreasing solvent concentration) as well as the surface tension σ (the surface tension increases with decreasing solvent concentration) and the evaporation rate e. The evaporation rate also depends on solvent concentration and on the height of the film, as a thin film dries fast due to its closeness to the warm substrate. We assume a well–mixed coating, where both components are transported by the same horizontal fluid velocity u.

This model can introduce micro structures even on an initially flat coating. Indeed, they may be originated in a inhomogeneous distribution of solvent. Local areas on the coating where the solvent concentration is high have less surface tension. This induces a Marangoni flow in the direction from high to low solvent concentration. This flow reduces the surface energy as the interface with less surface tension is strechted in comparison to the interface with high surface tension, which is condensed. Hence, fluctuation in the solvent concentration lead to a structured film height. On the other hand, surface tension primarily induces a flow which reduces the area of the interface. It therefore drives the fluid to a flat film. These two forces can in the absence of evaporation compensate each other leading to an inhomogeneous structured but stable film, c.f.[W93]. Figure 2 shows a Marangoni induced stable micro

structure.

Furthermore, the combination of a height dependent evaporation rate e of the solvent and of Marangoni effects (i.e. the solvent dependent surface tension) counteracts film rupture at points, where the height of the film tends to zero. In fact, due to their closeness to the warm surface the film dries quickly at low film heights. This reduces the solvent concentration at these points, which again induces a Marangoni flow to the valleys on the film surface due to a higher surface tension in case of a low solvent concentration. This flow counteracts rupture. Indeed our simulations (Figures 5 and 4) do not show a critical deepening of the film leading to rupture.

Gradient Flow Structure. For our model we firstly assume a balance of viscous and capillary forces but neglect the momentum of the fluid. We assume an over–damped limit in which the quasi stationary Stokes equations for an incompressible fluid are appropriate. By the well known lubrication approximation [BDO97] they can be reduced to the thin film equations, which are of gradient flow structure (cf. [GO03]). The height of the film h performs a steepest descent of an energy functional E:

$$\dot{h} = -\mathrm{grad}E\big|_h. \tag{1}$$

To make sense of the gradient of the energy one has to identify the metric structure of the manifold $\mathcal{M}$ on which the gradient flow takes place. In this case, this is the manifold of all heights of the film with prescribed volume. The metric is described by its metric tensor $g_h(\delta h, \delta h)$ on the tangent spaces, which consist of the infinitesimal height variations δh. Denoting $\mathrm{diff}E\big|_h.\delta h = \lim_{\varepsilon \to 0} \frac{1}{\varepsilon}(E(h + \varepsilon\delta h) - E(h))$ turns (1) into

$$g_h(\dot{h}, \delta h) = -\mathrm{diff}\,E\big|_h.\delta h \qquad \forall\,\delta h \in T_h\mathcal{M}. \tag{2}$$

Equation (2) can be seen as the Euler–Lagrange equation of

$$\mathcal{F}(\delta h) = \frac{1}{2}\,g_h(\delta h, \delta h) + \mathrm{diff}\,E\big|_h.\delta h \tag{3}$$

with respect to δh. Indeed, the actual rate of change $\dot{h}$ minimizes $\mathcal{F}$ under all possible infinitesimal variations δh. We will use such a gradient flow structure to model thin coatings, inspired by the gradient flow model for thin films, which we will explained first.

Thin Films as a Gradient Flow. Thin fluid films are described by the well known thin film equation

$$\dot{h} = -\frac{\sigma}{3\mu}\,\mathrm{div}(h^3\nabla\Delta h), \tag{4}$$

for the height of the film [BDO97]. Here, we might impose either periodic or natural boundary conditions. This evolution is a gradient flow, as introduced in [O01]. The relevant energy is the linearized surface energy:

$$E(h) := \int_\Omega \sigma \left(1 + \frac{1}{2} |\nabla h|^2 \right) dx.$$

The metric tensor is given by the minimal energy dissipated by viscous friction, i. e.

$$g_h \left(\delta h, \delta h \right) = \inf_u \left\{ \int_\Omega \frac{3\mu}{h} u^2 dx \right\},$$

where Ω is the underlying domain. Note that the metric tensor is base point dependent. The infimum is taken over any velocity profile u that realizes the given change in film height δh described by the transport equation

$$\delta h + \operatorname{div} \left(h \, u \right) = 0. \tag{5}$$

On the first sight the metric tensor seems to be a complicated object, as it involves the minimization of the viscous friction. Therefore finding the minimizer of the functional $\mathcal{F}$ in (3) requires to solve a nested minimization problem. This can be avoided, if one describes the tangent space, i.e. all infinitesimal changes in film height h, directly by an admissible velocity fields u via (5) (of course the same δh may be described by many u's). In this sense the metric tensor can be lifted onto the space of admissible velocities u:

$$g_h(u, u) = \int_\Omega \frac{3\mu}{h} u^2 dx. \tag{6}$$

Rewriting (3) leads to a formulation of the gradient flow as the evolution

$$\dot{h} + \operatorname{div} \left(h \, u^* \right) = 0, \tag{7}$$

where u^* minimizes the Rayleigh functional

$$\mathcal{F}(u) = \frac{1}{2} g_h(u, u) + \operatorname{diff} E\big|_h . u \tag{8}$$

over all fluid velocities u. Here $\operatorname{diff} E\big|_h . u$ is defined as $\operatorname{diff} E\big|_h . \delta h$ with δh satisfying (5). It is now easy to see that the gradient flow given by $(6) - (8)$ coincides with the evolution of the thin film equation (4). Indeed, we observe that u^* solves the Euler–Lagrange equation corresponding to the Rayleigh functional (8):

$$0 = g_h(u^*, u) + \operatorname{diff} E\big|_h . u = \int_\Omega \frac{3\mu}{h} u^* \cdot u \, dx - \int_\Omega \sigma \nabla h \nabla \operatorname{div}(h \, u) \, dx$$

for all test velocities u. For periodic or natural boundary conditions this immediately implies

$$u^* = \frac{\sigma h^2}{3\mu} \nabla \Delta h.$$

Finally, plugging u^* into (7) yields the thin film equation (4). The thin film is a special case of a thin coating, i.e. the one with constant solvent concentration. Numerical results for the spreading of a thin film are shown in Figure 1.

Thin Coatings as a Gradient Flow. The model for thin coatings is more difficult, as the state of the paint is not only described by its film height h but also by the solvent concentration s in the film. We assume a thin film model, which is inspired by the gradient flow described above. Here, we adopt a point of view developed in [GP05]: The gradient flow evolves on the manifold of all possible film heights. The solvent will be transported along with the fluid and is taken into account as a vector bundle on the manifold. At any given film height, there is a vector space of possible solvent concentrations, the fiber. They are not part of the manifold. The tangent spaces therefore consist only of the infinitesimal changes in film height δh. These are induced by a velocity u (as explained above):

$$\delta h + \operatorname{div}(h\,u) = 0 \tag{9}$$

The solvent concentration is transported by parallel transport. That is, we assume a mixed fluid, where the solvent is transported by the same velocity. As s is the concentration of solvent, the actual amount of solvent is given by $h\,s$. Therefore

$$\delta(hs) + \operatorname{div}(hs\,u) = 0. \tag{10}$$

This vector bundle construction to model an extra component slaved to the transport of the fluid was introduced in [GP05] for a thin film with surfactant. The gradient flow is now given by the reduced energy and the metric on the manifold. As in the thin film case, the relevant energy is the linearized surface energy:

$$E(h, s) := \int_\Omega \sigma(s) \left(1 + \frac{1}{2}\,|\nabla h|^2\right) dx. \tag{11}$$

The surface tension σ depends on the solvent concentration s. This introduces Marangoni effects to the model, which we see in a drying coating. The metric is given by the minimal energy dissipated by viscous friction, where the viscosity μ depends on the solvent concentration. The drying coating becomes hard. One has the metric tensor

$$g_{h,s}(u, u) = \int_\Omega \frac{3\mu(s)}{h} u^2 dx. \tag{12}$$

The gradient flow is (9) and (10) with the velocity field $u = u^*$, where u^* minimizes the Rayleigh functional

$$\mathcal{F}(u) = \frac{1}{2}\,g_{h,s}(u, u) + \operatorname{diff} E\big|_{h,s}.u \tag{13}$$

over all velocities u. This model is similar to the thin film model, but has included the solvent features of a thin coating. On the one hand it tries to minimize the (linearized) surface energy (11) by mean surface tension and Marangoni flows. They reduce the energy by elongating the surface with low surface tension. One the other hand the flow is hindered by viscous friction (12). The viscous friction increases as the evaporation continues (as $\mu(s)$ is an

increasing function). The only effect not yet modeled is the evaporation. On a continuous level this would include the modeling of the full vapor phase. On the discrete level the evaporation is included as a second step in an operator splitting method, see below.

1.2 Natural Time Discretization

Any gradient flow has a natural time discretization. It involves the natural distance function dist on the manifold $\mathcal{M}$ defined via

$$\operatorname{dist}^2(h_0, h_1) := \inf_{\gamma} \left\{ \left(\int_0^1 \sqrt{g_{\gamma(t)}(\dot{\gamma}, \dot{\gamma})} \, dt \right)^2 \right\},$$

with γ any smooth curve with $\gamma(0) = h_0$ and $\gamma(1) = h_1$. If $\mathcal{M}$ is actually Euclidean instead of genuinely Riemannian as in our case

$$\operatorname{dist}^2(h_0, h_1) = |h_0 - h_1|^2. \tag{14}$$

If τ denotes the time step size, the solution h^{k+1} at step $k+1$ can be inferred from the state h^k at step k via the variational problem:

$$h^{k+1} = \operatorname{argmin}_h \left\{ \frac{1}{2\tau} \operatorname{dist}^2(h, h^k) + E(h) \right\}. \tag{15}$$

As a motivation consider the Euclidean case (14). Here the Euler–Lagrange equation for (15) turns into the implicit Euler scheme

$$\frac{1}{\tau}(h^{k+1} - h^k) = -\nabla E\big|_{h^{k+1}}.$$

We want to use (15) as a starting point to construct a natural and stable discretization. The drawback of (15) is, it is fully nonlinear and it involves two nested minimizations.

One natural idea to overcome this drawback, which is also used for epitaxial growth, see the corresponding chapter in this book, is the following: We approximate the functional by its quadratic at h^k and then lift the variational problem on the level of possible velocities u in the spirit of (7) and (8). We first turn to the quadratic approximation: Writing $h = h^k + \tau \delta h$, we have

$$\frac{1}{2\tau} \operatorname{dist}^2(h, h^k) + E(h) \approx$$
$$\frac{\tau}{2} g_{h^k}(\delta h, \delta h) + E(h^k) + \tau \operatorname{diff} E\big|_{h^k}.\delta h + \frac{\tau^2}{2} g_{h^k}(\delta h, \operatorname{Hess} E\big|_{h^k} \delta h), \tag{16}$$

where $\operatorname{Hess} E\big|_{h^k}$ denotes the Hessian of E in h^k. Hence we can solve

$$\delta h^* = \operatorname{argmin}_{\delta h} \left\{ \frac{1}{2} g_{h^k}(\delta h, \delta h) + \operatorname{diff} E\big|_{h^k}.\delta h + \frac{\tau}{2} g_{h^k}(\delta h, \operatorname{Hess} E\big|_{h^k} \delta h) \right\} \tag{17}$$

and then set $h^{k+1} = h^k + \tau \delta h^*$, cf. (3). However, as in (3), (17) still involves two nested minimizations. Therefore, using (5) we may lift (17) on the level of possible velocities u as before. This yields

$$u^{k+1} = \operatorname{argmin}_u \left\{ \frac{1}{2} g_{h^k}(u, u) + \operatorname{diff} E\big|_{h^k}.u + \frac{\tau}{2} g_{h^k}(u, \operatorname{Hess} E\big|_{h^k} u) \right\} \tag{18}$$

and then set $h^{k+1} = h^k + \tau \operatorname{div}(h^k u^{k+1})$. Compare (18) to (7) and (8). This is the basis for the gradient flow algorithm used for epitaxial growth.

For our algorithm we use an alternative approach. We consider a semi implicit time discretization. For this we only approximate the squared distance dist^2 in (15) by its metric based approximation and keep E fully nonlinear. We use the following notation: For given velocity field u varying in space and fixed in time define the transport operator $\mathbf{h}(\cdot, \cdot)$, which maps a height field h^k at time t^k onto a height field $\mathbf{h}(h^k, u) = h(t^{k+1})$, where h solves the transport equation $\partial_t h + \operatorname{div}(h\, u) = 0$ with initial data $h(t^k) = h^k$. Given this operator, we again apply a linearization of the distance map dist in (15) and evaluate the energy on $\mathbf{h}[h_k, u]$. This energy is again implicitly defined via the velocity field u, which minimizes a corresponding functional. Thus, we define

$$u^{k+1} = \operatorname{argmin}_u \left\{ \frac{\tau}{2} g_{h^k}(u, u) + E(\mathbf{h}(h^k, u)) \right\}, \tag{19}$$

which can be considered as a semi-implicit alternative to the time discretization in (18). The new height field is then given by $h^{k+1} = \mathbf{h}(h^k, u^{k+1})$. Here, we still use the metric for the linearization of the distance map and evaluate this at the height field h^k at the old time t^k.

This gradient flow model for the thin film equation can easily be generalized for the thin coating model. To simplify the presentation let us introduce the vector $q = (h, hs)$ consisting of the two conservative quantities film height h and amount of solvent hs. Furthermore, we again define a transport operator $\mathbf{q}(\cdot, \cdot)$, which maps $q^k = (h^k, h^k s^k)$ at time t^k onto $\mathbf{q}(q^k, u) = q(t^{k+1})$, where q is a the solution of the system of transport equations

$$\partial_t h + \operatorname{div}(h\, u) = 0 \tag{20}$$
$$\partial_t(hs) + \operatorname{div}(hs\, u) = 0 \tag{21}$$

with initial data $q(t^k) = q^k = (h^k, h^k s^k)$. In analogy to (19), we consider an implicit variational definition of the motion field

$$u^{k+1} = \operatorname{argmin}_u \left\{ \frac{\tau}{2} g_{q^k}(u, u) + E(\mathbf{q}(h^k, u)) \right\}, \tag{22}$$

where $E[q]$ is given by (11). Hence, in every time step we ask for the minimizer of a functional whose integrand depends on the solution of a hyperbolic initial value problem. Indeed this is a PDE constrained optimization problem. In the next section we will solve this problem numerically based on a suitable space discretization and duality techniques.

1.3 Space Discretization for the Gradient Flow

Let us consider a discretization of (22) in one and two space dimensions and for simplicity restrict to a domain $\Omega = [0,1]^d$, where $d \in \{1,2\}$, and impose periodic boundary conditions. We suppose Ω to be regularly subdivided into N interval of width $\Delta := \frac{1}{N}$ (d=1) or squares of edge length Δ (d=2). By $Q = (Q_i)_{i \in I} = (H_i, H_i S_i)_{i \in I}$ and $U = (U_i)_{i \in I}$ we denote nodal vectors of discrete q and u quantities, respectively, where the ith component corresponds to a grid nodes x_i. Here I is supposed to be the lexicographically ordered index set of nodes (for $d = 2$ these indices are 2-valued, i. e. $i = (i_1, i_2)$, where the two components indicate the integer coordinates on the grid lattice). Spatial periodicity can be expressed by the notational assumption $Q_i = Q_{i+Ne}$ and $V_i = V_{i+Ne}$, where $e = 1$ for $d = 1$ and $e = (1,0)$ or $(0,1)$ for $d = 2$. Now, we define in a straightforward way a discrete energy value $E[Q]$ on $\mathbb{R}^{2\sharp I}$ and a discrete metric $G_Q[U,U]$ on $\mathbb{R}^{d\sharp I} \times \mathbb{R}^{d\sharp I}$:

$$E[Q] = \sum_{i \in I} \Delta^d \sigma(\tilde{S}_i) \left[1 + \frac{1}{2} (\nabla_i H)^2 \right], \tag{23}$$

$$G_Q(U,U) = \sum_{i \in I} \Delta^d \frac{3\mu(S_i)}{H_i} |U_i|^2, \tag{24}$$

where $\tilde{S} = \frac{1}{2}(S_i + S_{i+1})$ $(d = 1)$ or $\tilde{S} = \frac{1}{4}(S_i + S_{i+(0,1)} + S_{i+(1,0)} + S_{i+(1,1)})$ $(d = 2)$ are interpolated values for the solvent concentration at cell centers, and $\nabla_i H = \frac{1}{\Delta}(H_{i+1} - H_i)$ $(d = 1)$ or $\nabla_i H = \frac{1}{2\Delta}(H_{i+(1,0)} + H_{i+(1,1)} - H_i - H_{i+(0,1)}, H_{i+(0,1)} + H_{i+(1,1)} - H_i - H_{i+(1,0)})$ $(d = 2)$ is the difference quotient approximation of the gradient of the height field. Next, we define an operator $\mathbf{Q}$, which computes $\mathbf{Q}(Q^k, U) = Q^{k+1} = (H_i^k, H_i^k S_i^k)_{i \in I}$ as the solution of an implicit Lax-Friedrich scheme for the associated transport problem for given data Q^k at time t^k and a discrete velocity vector U. Let us detail this here in the one dimensional case, where we obtain the following system of equations

$$\frac{Q_i^{k+1} - Q_i^k}{\tau} = \frac{U_{i+1} Q_{i+1}^{k+1} - U_{i-1} Q_{i-1}^{k+1}}{2\Delta} + \epsilon \frac{Q_{i+1}^{k+1} - 2Q_i^{k+1} + Q_{i-1}^{k+1}}{\Delta^2}$$

for all $i \in I$ and a small positive constant ϵ. The two dimensional case is completely analogous. This scheme can be rewritten in matrix vector notation

$$Q^k = A(U)\mathbf{Q}(Q^k, U) \tag{25}$$

where $A(U) \in \mathbb{R}^{2\sharp I \times 2\sharp I}$ is a matrix depending on the discrete vector field U, which can easily be extracted from the Lax-Friedrich scheme. For $\epsilon > 0$ this matrix is invertible. Thus, we obtain the explicit representation $\mathbf{Q}(Q^k, U) = A(U)^{-1} Q^k$ for the discrete transport operator. With these ingredients at hand, one obtains a discrete counterpart of the variational problem (22)

$$U^{k+1} = \operatorname{argmin}_{U \in \mathbb{R}^{d\sharp I}} \left\{ \frac{\tau}{2} G_{Q^k}(U,U) + E(\mathbf{Q}(Q^k, U)) \right\}. \tag{26}$$

Finally, we define $Q^{k+1} = \mathbf{Q}(Q^k, U^{k+1})$. In each time step we aim at computing the discrete minimizer U^{k+1} via a gradient descent scheme on $\mathbb{R}^{d\sharp I}$. Hence, besides the energy on the right hand side of (26) we have to compute the gradient vector on $\mathbb{R}^{d\sharp I}$. For the variation of the energy $E(\mathbf{Q}(Q^k, U))$ in a direction $W \in \mathbb{R}^{d\sharp I}$ we get $\partial_U E(\mathbf{Q}(Q^k, U))(W) = \partial_Q E(\mathbf{Q}(Q^k, U))(\partial_U \mathbf{Q}(Q^k, U)(W))$. A direct application of this formula for the evaluation of the gradient of the energy E would require the computation of

$$\partial_U \mathbf{Q}(Q^k, U)(W) = -A^{-1}(U)(\partial_U A(U)(W))A^{-1}(U)Q^k$$

for every nodal vector W in $\mathbb{R}^{d\sharp I}$. To avoid this, let us introduce the dual solution $P = P(Q^k, U) \in \mathbb{R}^{2\sharp I}$ which solves

$$A(U)^T P = -\partial_Q E(\mathbf{Q}(Q^k, U)).$$

Computing the variation of the linear system (25) with respect to U we achieve

$$0 = (\partial_U A(U)(W))\mathbf{Q}(Q^k, U) + A(U)(\partial_U \mathbf{Q}(Q^k, U)(W)),$$

from which we then derive

$$\begin{aligned}
\partial_U E(\mathbf{Q}(Q^k, U))(W) &= \partial_Q E(\mathbf{Q}(Q^k, U))(\partial_U \mathbf{Q}(Q^k, U)(W)) \\
&= -A(U)^T P(Q^k, U) \cdot (\partial_U \mathbf{Q}(Q^k, U)(W)) \\
&= -P(Q^k, U) \cdot A(U)(\partial_U \mathbf{Q}(Q^k, U)(W)) \\
&= P(Q^k, U) \cdot (\partial_U A(U)(W))\mathbf{Q}(Q^k, U).
\end{aligned}$$

This representation of the variation of the energy can be evaluated without solving $d\sharp I$ linear systems of equations. In our implementation we consider the Armijo rule as a step size control in the descent algorithm on $\mathbb{R}^{d\sharp I}$.

1.4 Evolution of Thin Coatings with Solvent Evaporation

So far the model for the evolution of a thin film consisting of resin and solvent is considered as a closed system and formulated as a gradient flow. Evaporation of the solvent from the liquid into the gas phase - the major effect in the drying of the coating - still has to be taken into account. As already mentioned, incorporating this in a gradient flow formulation would require to model the gas phase as well. To avoid this we use an operator splitting approach and consider the evaporation separately as a right hand side in the transport equations. Thus, we consider the modified transport equations

$$\begin{aligned}
\partial_t h + \text{div}(h\,u) &= e(h, s)\,, \\
\partial_t (hs) + \text{div}(hs\,u) &= e(h, s)\,,
\end{aligned}$$

where $e(h, s) = -\frac{C}{c+hs}$ is the usual model for the evaporation [BDO97], where $C, c > 0$ are evaporation parameters. In the time discretization we now alternate the descent step of the gradient flow and an explicit time integration

of the evaporation. In the first step, the velocity u^{k+1} is computed based on (22) . Solving the corresponding transport equations (20) and (21) we obtain updated solutions for the height and the solvent concentration at time t^{k+1}, which we denote by $\tilde{h}^{k+1}$ and $\tilde{s}^{k+1}$, respectively. In the second step, applying an explicit integration scheme for the evaporation we finally compute

$$h^{k+1} = \tilde{h}^{k+1} + \tau e(\tilde{h}^{k+1}, \tilde{s}^{k+1}),$$
$$s^{k+1} = (h^{k+1})^{-1}(\tilde{h}^{k+1}\tilde{s}^{k+1} + \tau e(\tilde{h}^{k+1}, \tilde{s}^{k+1})).$$

For the fully discrete scheme, we proceed analogously and update the nodal values Q^{k+1} in each time step. In fact, given U^{k+1} as the minimizer of (26) we compute $\tilde{Q}^{k+1} = (\tilde{H}^{k+1}, \tilde{S}^{k+1}) = A(U^{k+1})^{-1}Q^k$ and then update pointwise $Q_i^{k+1} = \tilde{Q}_i^{k+1} + \tau e(\tilde{H}_i^{k+1}, \tilde{S}_i^{k+1})$.

1.5 Numerical Results

The numerical results show the features of thin coatings introduced by Marangoni and surface tension effects combined with evaporation and hardening. We will discuss them separately. A first test of our algorithm was to run it with constant solvent concentration, which turns the model for thin coatings into the simpler thin film model described above. Numerical results are already shown in Figure 1. They are numerically consistent with results obtained by a finite volume scheme for the thin film equation [GLR02], where thin films with (and without) surfactant are simulated. Figure 2 shows the effects introduced by Marangoni forces. In particular an inhomogeneous solvent concentration can lead to a structure formation in the film height. In the absence of evaporation this structure becomes stable as the Marangoni forces are opposed by mean surface tension forces, which want to reduce the length of the film surface.
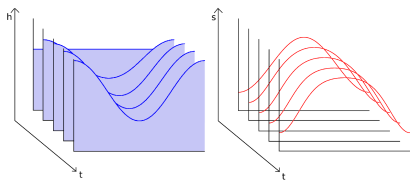

Fig. 2. Evolution of a coating with a marangoni flow introduced by an inhomogeneous solvent concentration.
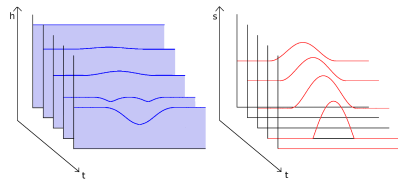
Fig. 3. Evolution of a coating with evaporating solvent.

An inhomogeneous solvent concentration also introduces a structured film height via evaporation, Figure 3. This leads - as only solvent evaporates - to valleys in the film located at positions with a high amount of solvent. Still the coating is by no means close to rupture, as this is opposed by Marangoni

forces. Figure 5 shows that the combination of these effects leads to a micro structure. This micro structures turns into a stable pattern of the dry coating. This is due to a solvent dependent viscosity, which leads to hardening during the drying process. Figure 4 shows that in a coating with constant viscosity the mean surface tension forces dominate the evolution at later times. This finally leads to a flat coating similar to the thin film case. Micro structures occur only at intermediate times.
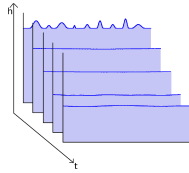

Fig. 4. The drying of a coating with (artifically) constant viscosity with a vanishing of micro structures.
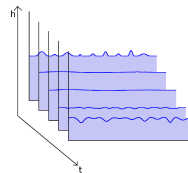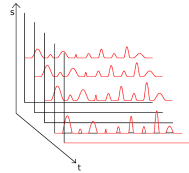
Fig. 5. The evolution of a coating with hardening, where micro structures persist.

2 Micro Structured Coatings and Effective Macroscopic Contact Angle

Micro structures in thin coatings are not only an unwanted feature, like the rupture of a coating. They also can be desirable, as micro structures enhance water repellent properties of a surface. This feature is known as the lotus effect. Among other plants, the lotus plant makes use of this [BN97], to let water roll off their leaves. One can also spot it at the back of a duck. The duck will stay dry while the water rolls off in pearls, as the feathers have a micro structure whose cavities are not filled with the water. To analyze this effect one has to understand how the form of the drops especially the contact angles are determined by the surface energy, which is the relevant energy in the quasi static case we are considering here.

The surface energy E is the sum of the energies of the three different interfaces in our problem. That is, the liquid/vapor interface Σ_{LV}, the solid/liquid interface Σ_{SL} and the solid/vapor interface Σ_{SV}. Each of these interfaces is weigthened with its surface tension:

$$E = |\Sigma_{SL}| \cdot \sigma_{sl} + |\Sigma_{LV}| \cdot \sigma_{lv} + |\Sigma_{SV}| \cdot \sigma_{sv}.$$

The shape of the drop is the one with the least energy given the volume of the drop. This also determines the contact angle, which is important to understand the lotus effect. Drops with large contact angles take a nearly pearl like form and roll of easily. Drops with small contact angles are flatter

and stick more to the surface.

For a flat surface the contact angle θ^Y can be calculated using Young's law, which can be derived from minimizing property with respect to the surface energy (see below):

$$\cos \theta^Y \;=\; \frac{\sigma_{sv} - \sigma_{sl}}{\sigma_{lv}}. \tag{27}$$

Drops on surfaces with micro structures are more complicated. They can either fill the micro structure with water, a situation described by Wenzel in [W36] (Figure 6), or they can sit on air bubbles situated in the surface cavities, as considered by Cassie and Baxter in [CB44], see Figure 7. For a nice review on this effect see either [Q02] or the book [GBQ04].
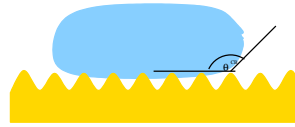

Fig. 6. A Wenzel type drop

Fig. 7. A Cassie–Baxter type drop

On a periodic surface it is possible to calculate effective contact angles. These are contact angles that would be attained in the limit of small scale periodicity. These contact angles determine the shape of the drop, see Figures 6 and 7. The micro structure is much smaller than the size of the drop. It therefore makes sense to think of an effective surface tension of the micro structured surface. The justification for this is given in [AS05], where it is shown that the energy minimizing drops behave in the limit of small surface periodicity like the drops with the corresponding effective surface tensions. This is a mathematically rigorous argument using the Γ-convergence of the energies.

The effective surface tensions are the ones assigned to a macroscopically flat surface with a small scale micro structure. In the Wenzel situation the solid surface and thereby the solid/liquid interface as well as the solid/vapor interface are enlarged by the roughness r. (r equals the area of the surface on the unit square.) The effective surface tensions σ_{sl}^* and σ_{sv}^* are:

$$\sigma_{sl}^* \;=\; r \cdot \sigma_{sl} \qquad \text{and} \qquad \sigma_{sv}^* \;=\; r \cdot \sigma_{sv},$$

The effective contact angle θ^W is then determined by an adapted Young's law, cf. (27):

$$\cos \theta^W \;=\; \frac{\sigma_{sv}^* - \sigma_{sl}^*}{\sigma_{lv}} \;=\; r \cdot \frac{\sigma_{sv} - \sigma_{sl}}{\sigma_{lv}}.$$

Therefore a Wenzel type situation enlarges large contact angles and shrinks small ones in comparison to the flat surface case. Thus it enhances water repellent properties of a surface (with pearl like drops and large contact angles),

as well as hydrophilic properties (with flat drops and low contact angles). In the Cassie–Baxter situation the calculation of the effective surface tension is more difficult as it involves a determination of the size of the vapor bubbles at the micro scale, see Figure 7. In a periodic set up this leads to a free boundary problem to be solved on the periodicity cell. The solution may be a configuration with or without vapor inclusions. At the triple line the contact angle for a flat surface θ^Y is attained. Below, we developed an algorithm which solves the free boundary problem and thereby determines the shape of the vapor inclusions.
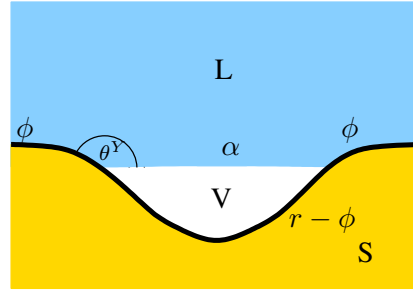

Fig. 8. The Configuration of a cell problem in the Cassie–Baxter regime.

The solution of the cell problem provides the area α of the liquid/vapor interface in one periodicity cell, the area β of the solid/liquid interface and the area of the solid/vapor interface, which is $r - \beta$, see figure 8. The effective surface tension $\sigma^\star_{sl}$ is the sum of the surface tensions of the interfaces:

$$\sigma^\star_{sl} = \alpha \cdot \sigma_{lv} + \beta \cdot \sigma_{sl} + (r - \beta) \cdot \sigma_{sv}.$$

We obtain a modified Young's law (cf. (27)) for the effective solid/vapor surface tension $\sigma^\star_{sv} = r \cdot \sigma_{sv}$ and thereby determine the effective Cassie–Baxter contact angle:

$$\cos \theta^{CB} = \frac{\sigma^\star_{sv} - \sigma^\star_{sl}}{\sigma_{lv}} = -\alpha + \beta \cdot \cos \theta^Y.$$

For $\alpha \to 1$ and $\beta \to 0$ the Cassie–Baxter contact angle tends to 180°. This is the situation when the drop hardly touches the surface but rests mostly on the air pockets. The drop takes a nearly spherical shape and rolls off easily.

The effective contact angles calculated above are derived under the assumption of periodicity of the surface. An assumption typically not satisfied by natural surfaces. Theses surfaces show a highly inhomogeneous structure with both sizes and shape of the micro structure varying over several orders of magnitude, see Figure 9. A future perspective is to derive a mathematical model which captures these inhomogeneities. It should be based on a stochastical model where one asks for the expectation of the effective contact angle.
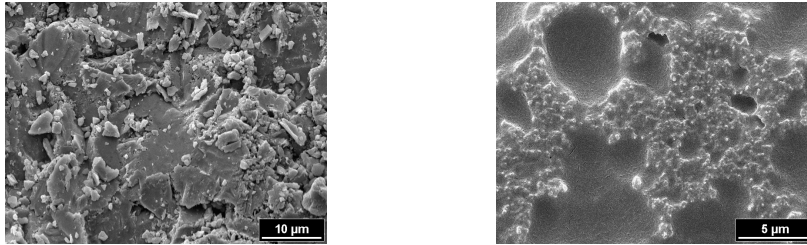
Fig. 9. Natural surfaces with micro structure (copyright: Bayer Material Science)

There is a second drawback of Young's law which describes the the absolut minimizer of the energy. In fact, drops on surface can have many different stable contact angles. Rain drops on a window sheet demonstrate this in our daily life. They stick to the window and do not roll off, in spite of the window being inclined. These drops are not spherical caps but take an non symmetric shape, see Figure 10.
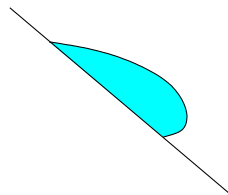

Fig. 10. A drop sticking to a tilted plane

The contact angles at the upward point part of the contact line are much smaller than those at the downward pointing part. Nevertheless all contact angles are stable, as the drop does not move. We developed a new model to understand which drops are stable, [SGO07], see Section 2.2. This model is adapted from models used in dry friction and elasto–plasticity. It mainly states that a drop should by stable, if the energy landscape is not to steep at its configuration.

2.1 Computing the Effective Contact Angle

In this section we will discuss how to compute the effective contact angle on a rough coating surface in the regime of the Cassie–Baxter model. Thus, we consider a periodic surface micro structure described by a graph on a rectangular fundamental cell Ω (cf. Fig. 11). The surface itself is supposed to be given as a graph $f : \Omega \to \mathbb{R}$, whereas the graph of a second function $u : \Omega \to \mathbb{R}$ represents the gas / liquid interface between a vapor inclusion on the surface and the covering liquid. In fact, we suppose $\{(x, y) \in \Omega \times \mathbb{R} \,|\, f(x) <$

$y < u(x)\}$ to be the enclosed gas volume. Following [SGO07] we take into acount the total (linearized) surface energy on the cell Ω given by

$$
\begin{aligned}
E(u, f) &= \int\limits_{[u>f]} \sigma_{sv}\sqrt{1+|\nabla f|^2} + \sigma_{lv}\sqrt{1+|\nabla u|^2}\mathrm{d}x + \int\limits_{[u<f]} \sigma_{sl}\sqrt{1+|\nabla f|^2}\mathrm{d}x \\
&= \int\limits_{[u>f]} (\sigma_{sv}-\sigma_{sl})\sqrt{1+|\nabla f|^2} + \sigma_{lv}\sqrt{1+|\nabla u|^2}\mathrm{d}x \\
&\quad + \int\limits_{\Omega} \sigma_{sl}\sqrt{1+|\nabla f|^2}\mathrm{d}x
\end{aligned}
$$

Here, $[u > f] = \{x \in \Omega \,|\, f(x) < u(x)\}$ represents the non wetted domain of the vapor inclusion, also denoted by Ω_{sv}, and $[u < f] = \{x \in \Omega \,|\, f(x) > u(x)\}$ the wetted domain, respectively (cf. Fig. 7, 11). Let us emphasize that for fixed f the energy effectively depends only on $u|_{[u>f]}$. In the energy minimization we have to compensate for this by a suitable extension of u outside $[u > f]$. The variation of the energy E with respect to u in a direction w is given by

$$
\begin{aligned}
\partial_u E(u, f)(w) &= \int\limits_{\partial[u>f]} (v \cdot \nu)\left((\sigma_{sv}-\sigma_{sl})\sqrt{1+|\nabla f|^2} + \sigma_{lv}\sqrt{1+|\nabla u|^2}\right)\mathrm{d}\mathcal{H}^1 \\
&\quad + \int\limits_{[u>f]} \sigma_{lv}\frac{\nabla u \cdot \nabla w}{\sqrt{1+|\nabla u|^2}}\mathrm{d}x\,,
\end{aligned}
$$

where ν denotes the outer normal at the triple line $\partial[u > f]$ and v is the normal velocity field of this interface induced by the variation w of the height function u. The relation between $v \cdot \nu$ and w is given by $(v \cdot \nu)(\nabla f \cdot \nu - \nabla u \cdot \nu) = w$. A minimizer u of $E(\cdot, f)$ describing the local vapor inclusion attached to the surface is described by the necessary condition $\partial_u E(u, f)(w) = 0$ for all smooth variations w. Applying integration by parts we deduce the minimal surface equation $-\mathrm{div}\frac{\nabla u}{\sqrt{1+|\nabla u|^2}} = 0$ for u on $[u > f]$ and the boundary condition

$$
0 = \frac{(\sigma_{sv}-\sigma_{sl})\sqrt{1+|\nabla f|^2} + \sigma_{lv}\sqrt{1+|\nabla u|^2}}{\nabla f \cdot \nu - \nabla u \cdot \nu} + \frac{\sigma_{lv}\nabla u \cdot \nu}{\sqrt{1+|\nabla u|^2}}
$$

on $\partial[u > f]$. The energy is invariant under rigid body motions. Hence, for a point x on $\partial[u > f]$ we may assume $\nabla f(x) = 0$. In this case $\nu(x) = -\frac{\nabla u(x)}{|\nabla u(x)|}$ and thus $\frac{\sigma_{ls}-\sigma_{sv}}{\sigma_{lv}} = \sqrt{1+|\nabla u(x)|^2} - \frac{|\nabla u(x)|^2}{\sqrt{1+|\nabla u(x)|^2}} = \frac{1}{\sqrt{1+|\nabla u(x)|^2}} = \cos(\theta)$, where θ is the contact angle between the solid-liquid and the liquid vapor interface. Hence, we have recovered Young's law on the micro scale of the cell problem.

Finally we end up with the following free boundary problem to be solved: Find a domain Ω_{sv} and a function u, such that the graph of u on Ω_{sv} is a minimal

surface with Dirichlet boundary condition $u = f$ and prescribed contact angle θ on $\partial\Omega_{sv}$, and this graph should be periodically extendable as a continuous graph on $\mathbb{R}^2$ (cf. Fig. 11 and Fig. 12).
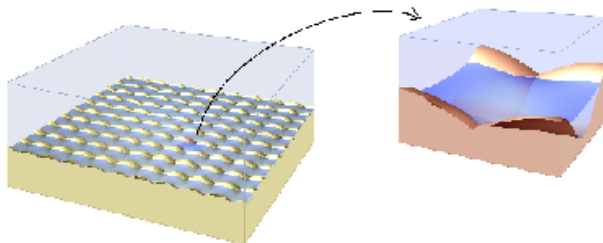

Fig. 11. The effective contact angle on a rough surface is calculated based on the numerical solution of a free boundary problem on a fundamental cell. The liquid vapor interface of the vapor inclusion on the surface forms a minimal surface with a contact angle on the surface of the solid determined by Young's law.
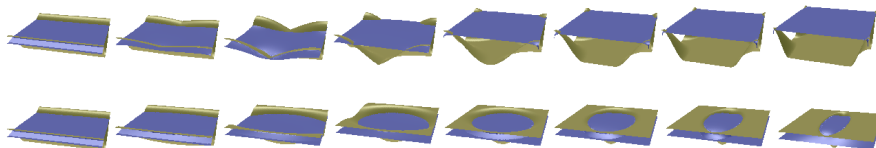

Fig. 12. Each row shows on the periodic cell a family of coating surfaces together with the liquid vapor interfaces of the corresponding vapor inclusions in the wetting regime of the Cassie–Baxter model. In the first row the transition in the surface configuration from a wavelike pattern in one axial direction to more spike type structures is depicted from left to right, whereas in the second row the transition from the same wave pattern to elongated troughs is shown.

The numerical solution of this free boundary problem is based on a time discrete gradient descent approach for a suitable spatially discrete version of the above variational problem. Let us denote by $\mathcal{V}_h$ the space of piecewise affine, continuous functions (with a continuous periodic extension on $\mathbb{R}^2$ on some underlying simplicial mesh of grid size h covering the rectangular fundamental cell Ω. For a discrete graph $F \in \mathcal{V}_h$ of the coating surface we start from some initial guess $U^0 \in \mathcal{V}_h$ for the (extended) discrete graph of the liquid vapor interface on top of the vapor inclusions and successively compute a family $(U^k)_{k \geq 0}$ with decreasing Energy $E(\cdot, F)$. For given U^k we first solve the discrete Dirichlet problem for a minimal surface on $\Omega_{sv}^k := [U^k > F]$ in a composite finite element space $\mathcal{V}_h^k$ [HS97, HS98] and based on that compute the next iterate U^{k+1}. In fact, following [HS97a] we define $\mathcal{V}_h^k$ as a suitable

subspace of functions $W \in \mathcal{V}_h$ with $W = 0$ on $\partial \Omega_{sv}^k$. Thereby, the degrees of freedom are nodal values on the original grid contained in Ω_{sv}^k whose distance from $\partial \Omega_{sv}^k$ is larger than some $\epsilon = \epsilon(h) > 0$. Then, a constructive extension operation defines nodal values on all grid nodes of cells intersec ted by Ω_{sv}^k (for details we refer to [HS97a]). Hence, we compute a solution $\tilde{U}^{k+1}$ with $\tilde{U}^{k+1} - F \in \mathcal{V}_h^k$, such that

$$0 = \int_{\Omega_{sv}^k} \frac{\nabla \tilde{U}^{k+1} \cdot \nabla \Phi}{\sqrt{1 + |\nabla U^k|^2}} \mathrm{d}x$$

for all test functions $\Phi \in \mathcal{V}_h^k$. Next, based on $\tilde{U}^{k+1}$ data on $\partial \Omega_{sv}^k$ we compute a discrete descent direction $V^k \in \mathcal{V}_h$ as the solution of

$$G^k(V^{k+1}, \Phi) = -\partial_u E(\tilde{U}^k, F)(\Phi)$$

for all $\Phi \in \mathcal{V}_h$. Here, with the intention of a proper preconditioning of the gradient descent, we take into account the metric $G^k(\Psi, \Phi) = \sigma_{lv} \int_{\Omega_{sv}^k} \frac{\nabla \Psi \cdot \nabla \Phi}{\sqrt{1 + |\nabla U^k|^2}}$.
Given V^{k+1} we finally determine the actual descent step applying Amijos step size control rule and compute $U^{k+1} = \tilde{U}^{k+1} + \tau^{k+1} V^{k+1}$ for a suitable timestep τ^{k+1}. Here, we implicitly assume that the built–in extension of $\tilde{U}^{k+1}$ on whole Ω is sufficiently smooth.

2.2 A New Model for Contact Angle Hysteresis

We consider a drop on a micro structured plane. Experiments show that there is an hysteresis interval $[\theta^r, \theta^a]$ of stable contact angles. It is bounded by the receding contact angle θ^r and the advancing contact angle θ^a. The dependence of this interval on the surface roughness is badly understood. We introduced a new model for contact angle hysteresis [SGO07] to understand the experimental evidence of a complicated dependence of the hysteresis interval on the roughness:
Well known experiments from the sixties [JD64] show that the width as well as the position of the hysteresis interval depend in a nonlinear way on the surface roughness, see Figure 13. Especially the receding contact angle shows a jump like behavior at a certain surface roughness.
Furthermore, recent experiments [QL03] show that the receding contact angle not only depends on the surface roughness, but also on the way the drop is put on the surface. In Figure 14 we show how the receding contact angles depends on a pressure applied to press the drop into surface cavities. The pressure is then released and the contact angle is measured. Figure 14 again shows a jump like behavior of the receding contact angle.

We introduce a new model to capture these phenomena. It is similar to models used in dry friction [MT04] and elasto–plasticity [MSM06]. The main idea of our model is that stability of drops is primarily not related to global or local
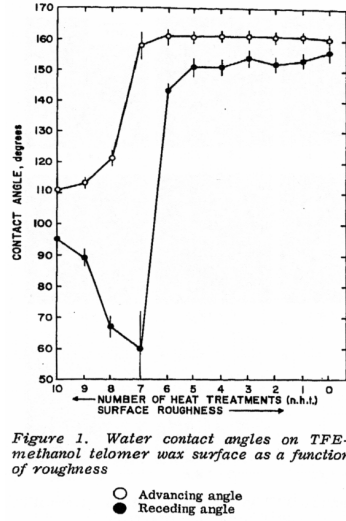
Figure 1. Water contact angles on TFE-
methanol telomer wax surface as a function
of roughness

 ○ Advancing angle
 ● Receding angle

Fig. 13. Experimental Dependence
of Advancing and Receding Contact
Angles on the Surface Roughness.
**Reprinted with Permission from
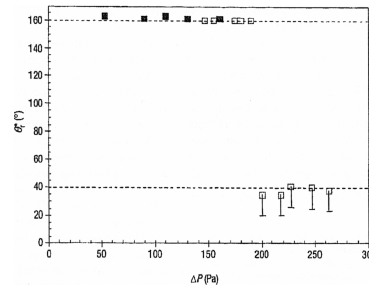[JD64]. Copyright (1964) Amer-
ican Chemical Society**

Fig. 14. Experimental Dependence of
Receding Contact Angles on the Pres-
sure Pushing the Drop onto the Sur-
face. Reprinted from [QL03] with Per-
mission.

minimality of its interfacial energy, but rather to the fact that the local energy–
landscape seen by the drop should not be too steep such that dissipation
energy pays off the modify the configuration. To be be more precise, if the
energy that would be gained moving the drop (i.e. controlled up to first order
by the slope of the energy landscape) is smaller than the energy that would be
dissipated while moving, then the drop will not move. In order to implement
these concept, we use the derivative–free framework proposed in [MM05] (see
also the review [M05]).

That is, we assume a drop L_0 (with its contact angle) to be stable if

$$E(L_0) \, - \, E(\tilde{L}) \, \leq \, dist(L_0, \tilde{L})$$

for all $\tilde{L}$ with the same volume. Here we have modeled the distance of two
drops to be the area of the coating surface wetted by only one of them. This
seems reasonable, as we know that the most energy is dissipated around the
moving triple line. Therefore a drop which has significantly changed its bot-
tom interface on the coating surface is far apart from its initial configuration.
Our new model implies two different diagrams of stable contact angles, de-
pending on the type of drop (Wenzel or Cassie–Baxter type). These are shown
in Figures 15 resp. 16 in the case of a surface with flat plateau and vallees,
separated by steep edges. The roughness of this type of surface can be in-

creased by deepening the asperities without changing the size of the wetted surface plateau. The hysteresis interval for Cassie–Baxter drops is much nar-
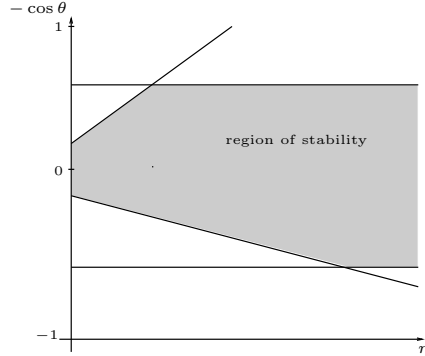

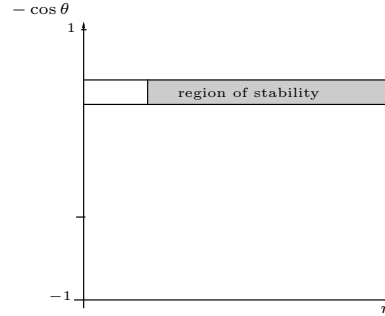**Fig. 15.** Stable contact angles for Wenzel type drops.

Fig. 16. Stable contact angles for Cassie–Baxter type drops.

rower than the one for Wenzel drops. This can explain qualitatively both the downward jump at large pressures of the receding contact angles in Figure 14, and the jump behavior in Figure 13.

The latter can be understood as a superposition of the two stability diagrams. The jump in the width of the hysteresis interval results from a transition from Wenzel type drops to Cassie–Baxter type drops. At low surface roughnesses Wenzel type drops are stable. They exhibit a wide hysteresis interval. At higher roughness, the stable configurations in the experiment are instead Cassie–Baxter. They display a much narrower hysteresis interval. The stable contact angles resulting from the transition from Wenzel to Cassie–Baxter drops are shown schematically in Figure 17, where they are superposed on the experimental results of Johnson and Dettre. The comparison is only qualitative, because experimentally roughness is measured only indirectly, through the number of heat treatments undergone by the solid surface in the sample preparation. The figure shows a transition from a regime in which the difference between advancing and receding contact angles increases monotonically with roughness, to one in which such a difference is smaller, and nonsensitive to roughness.

Figure 14 reflects the fact that the stability interval depends on the type of drop. Assuming that the corresponding surface has sufficiently large roughness, we see from Figures 15 and 16 that forcing a transition from a Cassie–Baxter to a Wenzel type drop (by applying a large enough pressure) may reduce the lower end of the stability interval (i.e., the receding contact angle) from well above to well below 90°.
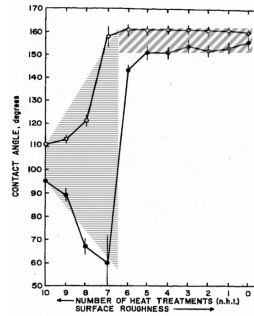
Fig. 17. A schematic sketch of the stable contact angles is given according to our model. The shaded regions represents the set of stable angles for varying surface roughness, superposed on experimental data from Figure 13.

References

[AS05] Alberti, G., DeSimone, A.: Wetting of rough surfaces: a homogenization approach. Proc. R. Soc. London Ser. A Math. Phys. Eng. Sci., **4**61, 79–97, (2005)

[BN97] Barthlott, W., Neinhuis, C.: Characterization and Distribution of Water–repellent, Self–cleaning Plant Surfaces. Annals of Botany, **7**9, 667–677, (1997)

[BGLR02] Becker, J., Grün, G., Lenz, M., Rumpf, M.: Numerical Methods for Fourth Order Nonlinear Degenerate Diffusion Problems. Applications of Mathematics, **47**, 517–543, (2002)

[CB44] Cassie, A.B.D., Baxter, S.: Wettability of Porous Surfaces. Trans. Faraday Soc., **40** , 546–551, (1944)

[MSM06] Dal Maso, G., DeSimone, A., Mora, M.G.: Quasistatic evolution problems for linearly elastic–perfectly plastic materials. Arch. Rat. Mech. Anal., **1**80, 237–291, (2006)

[GBQ04] de Gennes, P.G., Brochard-Wyart, F., Quéré, D.: Capillarity and Wetting Phenomena. Springer (2004)

[SGO07] DeSimone, A., Grunewald, N., Otto, F.: A new model for contact angle hysteresis. Networks and Heterogeneous Media, **2**, 2, 211–225, (2007)

[JD64] Dettre, R.H., Johnson, R.E.: Contact Angle Hysteresis II. Contact Angle Measurements on Rough Surfaces. Contact Angle, Wettability and Adhesion, Advances in Chemistry Series, **43**, 136–144, (1964)

[GO03] Giacomelli, L., Otto, F.: Rigorous lubrication approximation. Interfaces and Free boundaries, **5**, No. 4, 481–529, (2003)

[GP05] Günther, M., Prokert, G.: On a Hele–Shaw–type Domain Evolution with convected Surface Energy Density. SIAM J. Math. Anal., **37**, No. 2, 372–410, (2005)

[GLR02] Grün, G.,Lenz, M., Rumpf: A Finite Volume Scheme for Surfactant Driven Thin Film Flow. in: Finite volumes for complex applications III, M. Herbin, R., Krner, D. (ed.), Hermes Penton Sciences, 2002, 567-574

[HS97] Hackbusch, W. and Sauter, S. A.: Composite Finite Elements for Problems Containing Small Geometric Details. Part II: Implementation and Numerical Results. Comput. Visual. Sci., **1** 15–25, (1997)

[HS97a] Hackbusch, W. and Sauter, S. A.: Composite Finite Elements for problems with complicated boundary. Part III: Essential boundary conditions. technical report, Universität Kiel, (1997)

[HS98] Hackbusch, W. and Sauter, S. A.: A New Finite Element Approach for Problems Containing Small Geometric Details. Archivum Mathematicum, **3**4 105-117, (1998)

[HMO97] Howison, S.D., Moriarty, J.A., Ockendon, J.R., Terril, E.L., Wilson, S.K.: A mathematical model for drying paint layers. J. of Eng. Math., **3**2, 377–394, (1997)

[QL03] Lafuma, A., Quéré, D.: Superhydrophobic States. Nature Materials, **2**, 457–460, (2003)

[MM05] Mainik, A., Mielke, M.: Existence results for energetic models for rate–independent systems. Calc.Var., **2**2, 73–99, (2005)

[M05] Mielke, M.: Evolution of rate–independent systems. Handbook of Differential Equations. Evolutionary Equations, **2**, 461–559, (2005)

[MT04] Mielke, M., Theil, F.: On rate independent hysteresis models. NoDEA **1**1, 151–189, (2004)

[BDO97] Bankoff, S.G, Davis, S.H., Oron, A.: Long–scale evolution of thin liquid films. Rev. of modern Physics, **6**9, No. 3, 931–980, (1997)

[O01] Otto, F.: The geometry of dissipative evolution equations: the porous medium equation. Comm. Partial Differential Equations, **2**6, No.1-2, 101–174, (2001)

[Q02] Quéré, D.: Rough ideas on wetting. Physica A, **313**, 32–46, (2002)

[W36] Wenzel, R.N.: Resistance of Solid Surfaces to Wetting by Water. Ind. Eng. Chem., **2**8, 988–994, (1936)

[W93] Wilson, S.K.: The levelling of paint films. Journal of Applied Mathematics, **5**0, 149–166, (1993)